

Katabatic and convective processes drive two preferred peaks in the precipitation diurnal cycle over the Central Himalaya

Kieran M. R. Hunt¹, Andrew G Turner¹, and Reinhard K H Schiemann¹

¹University of Reading

November 23, 2022

Abstract

The diurnal cycle of precipitation over the Central Himalaya is governed by a complex interaction between the diurnal cycle of tropical convection and local orographic flow. Understanding this interaction is crucial for model evaluation, where the simulation of such processes is highly sensitive to model resolution and choice of parameterisation schemes. In this study, the mean diurnal cycle is computed using GPM-IMERG data and is shown to be bimodal, with one peak in the late afternoon (1700 LT) and a stronger one in the early morning (0200 LT). This structure is an artefact of compositing, as individual days are typically associated with single peaks. The late afternoon ‘convective’ peak is shown to be linked to the diurnal cycle of tropical convection, whereas the early morning ‘katabatic’ peak is shown to be triggered by nocturnal downslope flow converging with the background monsoon circulation. As such, the katabatic peak is strongly favoured by an active monsoon trough, which provides greater southeasterly moisture flux to the foothills, resulting in increased low-level moisture flux convergence upon interaction with the katabatic northerlies. In contrast, when the trough is less active, precipitation is brought to the region by mesoscale convective systems, ranging in scale from tens to thousands of kilometres, resulting in convective peaks. We hypothesise that these peaks may be enhanced by anabatic flow. It is shown that the BSISO does not play a significant role in modulating either the timing or amplitude of the diurnal cycle; however, low-pressure systems do: either by intensifying the trough (and hence the katabatic peak), or, when further north, by providing deep convection (hence supporting the convective peak). Reanalyses and a 17-km model with parameterised convection capture both peaks, but overestimate the magnitude of the convective peak and underestimate the magnitude of the katabatic peak.

Katabatic and convective processes drive two preferred peaks in the precipitation diurnal cycle over the Central Himalaya

Kieran M. R. Hunt^{1,2} | Andrew G. Turner^{1,2} | Reinhard
K. H. Schiemann^{1,2}

¹Department of Meteorology, University of Reading, United Kingdom

²National Centre for Atmospheric Science, University of Reading, United Kingdom

The diurnal cycle of precipitation over the Central Himalaya

Correspondence

Kieran M R Hunt, Department of Meteorology, Whiteknights Campus, University of Reading, RG6 6BB, United Kingdom
Email: k.m.r.hunt@reading.ac.uk

Funding information

is governed by a complex interaction between the diurnal cycle of tropical convection and local orographic flow. Understanding this interaction is crucial for model evaluation, where the simulation of such processes is highly sensitive to model resolution and choice of parameterisation schemes. In this study, the mean diurnal cycle is computed using GPM-IMERG data and is shown to be bimodal, with one peak in the late afternoon (1700 LT) and a stronger one in the early morning (0200 LT). This structure is an artefact of compositing, as individual days are typically associated with single peaks. The late afternoon 'convective' peak is shown to be linked to the diurnal cycle of tropical convection, whereas the early morning 'katabatic' peak is shown to be triggered by nocturnal downslope flow converging with the background monsoon circulation. As such, the katabatic peak is strongly favoured by an active monsoon trough, which provides greater southeasterly moisture flux to the foothills, resulting in increased low-level moisture flux convergence upon interaction with the katabatic northerlies. In contrast, when the trough is less active, precipitation is brought to the region by mesoscale convective systems, ranging in scale from tens to thousands of kilometres, resulting in convective peaks. We hypothesise that these peaks may be enhanced by anabatic flow. It is shown that the BSISO does not play a significant role in modulating either the timing or amplitude of the diurnal cycle; however, low-pressure systems do: either by intensifying the trough (and hence the katabatic peak), or, when further north, by providing deep convection (hence supporting the convective peak). Reanalyses and a 17-km model with parameterised convection capture both peaks, but overestimate the magnitude of the convective peak and underestimate the magnitude of the katabatic peak.

KEYWORDS

diurnal cycle, Himalaya, precipitation, orographic, convection

1 | INTRODUCTION

Over much of monsoonal India, the diurnal cycle of precipitation is dominated by tropical convection: solar heating warms the surface, which then warms and moistens the boundary layer through sensible and latent heat transfer. Eventually, the updrafts become strong enough to overcome convective inhibition and, by the late afternoon, deep convection is widespread. This picture gets increasingly complicated near the coasts – where the land-sea breeze plays an important secondary role – and near the Himalaya – where localised dynamics such as the nocturnal jet can dramatically alter atmospheric stability. It is this latter problem that is the focus of this study.

A full understanding of the processes at play, and how they interact with each other to produce the observed diurnal cycle across the Himalaya, is vital for model evaluation. In particular, parameterisation of these localised processes (e.g. to represent convection or subgrid orography) can lead to significant biases even on the synoptic scale. Marsham et al. (2013) showed that in simulations of the West African monsoon, parameterised convection occurred too early in the day, leading to mistimed feedbacks between radiative heating, latent heating and the meridional pressure gradient. This resulted in a much poorer simulation of the monsoon circulation than a parallel run with explicit convection. More generally, coarse-resolution models with parameterised convection tend to rain too early in the tropics and this premature initiation suppresses the build-up of CAPE, resulting in too light and too frequent rainfall over tropical land, with similar implications for the simulation of monsoonal circulation (Dai and Trenberth, 2004).

1.1 | The observed diurnal cycle of precipitation over the Himalaya

Satellite-based precipitation products have allowed a near-global assessment of the diurnal cycle of precipitation. Kikuchi and Wang (2008) showed that the strongest diurnal cycle exists over tropical land, where the peak (1500 local solar time – or LT) usually matched local heating. They also found that near large mountain ranges, the peak tended to be in the local early morning. This was corroborated by Sahany et al. (2010) who used spectral analysis to draw out the diurnal cycle over nine years of TRMM data over India. They found that inland, away from the coasts or orography, the rainfall peaked at 1430 LT; however, this was later over the Western Ghats (1430–1730 LT) and much earlier over the Himalayan foothills, where they recorded a single peak at 0230 LT. More recently, Watters et al. (2021) expanded these results for GPM-IMERG, ERA5, and three CMIP6 AMIP models. They found that IMERG also captured an early morning precipitation maximum over the Himalaya, with a cross-slope gradient (earlier maximum at higher altitudes), as well as a late afternoon maximum both further south (over the Indo-Gangetic Plain) and further north (over the Tibetan Plateau). The ERA5 reanalysis was able to capture most of these features, but had a late afternoon peak over much of the Himalaya.

More directed studies, combining satellite data with ground-based observations, have reached similar conclusions. Barros et al. (2000) explored the diurnal cycle of precipitation over Nepal for a single monsoon season. They found that the diurnal cycle was often bimodal, with a late afternoon and an early morning peak, though in the valleys, only the early morning peak was present. This was later complemented by a longer radiosonde campaign (Barros and Lang, 2003). Similarly, Bhatt and Nakamura (2006) explored the diurnal cycle over the Himalayas in a range of data sources, finding a mid-afternoon peak in the pre-monsoon and an early morning peak during the monsoon.

1.2 | Proposed mechanisms

Fitzjarrald (1984) constructed a one-dimensional model of katabatic winds in ambient flow. He found that the onset

time of katabatic (i.e. nocturnally-forced downslope) winds is sensitive to opposing flow and reduced cooling rates (e.g. from monsoon cloudiness). Over the Central Himalaya, the katabatic winds are northerly, and the opposing flow is thus the local southeasterly monsoonal circulation. The model had about an eight hour delay between sunset and the initiation of katabatic flow over humid tropical slopes, but, because it was one-dimensional, missed the effects of local convergence due to local topography. He also found that entrainment into katabatic winds might be an important control on downslope initiation of precipitation. Bluestein (1993) suggested that the nocturnal low-level jet that arises in response to differential heating/cooling across the orographic gradient could advect moisture into such a region, causing the early morning precipitation maximum seen in the Rockies. Using an intensive sonde and observation campaign over central Nepal, and supported by the NCEP/NCAR reanalysis, Barros and Lang (2003) found that precipitable water peaked around midnight, slightly after CAPE. They found that anabatic winds were more intense than katabatic winds, in agreement with many previous studies (Egger et al., 2000; Ueno et al., 2001; Bollasina et al., 2002) as well as Fitzjarrald (1984), as climatological monsoon winds are directed slightly upslope. They argued that convergence along the foothills was reduced during the day because of anabatic flow, favouring increased convergence at night (when the flow was katabatic). This way, as the monsoon continues to moisten the boundary layer, instability builds up during the whole day before it is finally released during the nocturnal precipitation. Barros and Lang (2003) found little evidence of a nocturnal low-level jet, but noted that this may have been due to the data sparsity of the region. Bhatt and Nakamura (2006) analysed the diurnal cycle using a combination of TRMM, radiosonde data, and two reanalyses. Following Fitzjarrald (1984), they attributed the early morning maximum to convergence from the interaction between katabatic flow and the southeasterly moisture flux of the summer monsoon. They further suggested that the radiative cooling at top of clouds may be an important driver and found that the cross-slope gradient in peak timing could be explained by cold pool density currents moving downslope, causing southward movement of precipitation systems in the morning. They also hypothesised that convection over the foothills could be triggered by gravity waves generated in response to the Himalaya acting to block the monsoon flow, arguing that this effect would be strongest in the early morning.

Indeed, R  thrich et al. (2013) found that maximum cloudiness over the Central Himalayan foothills occurred at 0200 LT but hypothesised that this was due to katabatic flow helping initiate mesoscale convective systems. Other studies have also investigated satellite-derived cloud data over the Himalaya to improve understanding of the diurnal cycle. Barros et al. (2004) found a strong link between cloudiness and precipitation over the Himalaya at all scales, from the synoptic, which they linked to mesoscale convective systems (MCSs) and monsoon depressions, to the mesoscale, which they linked to valleys and ridges in the orography. They found that the timing of heavy precipitation over the Himalaya was driven on the synoptic scale (which they defined as larger than 70 km), although convective cloud clusters are comparatively rare there compared to the Indo-Gangetic Plain and the Tibetan Plateau. Analysing extreme convection over the whole of South Asia, using the TRMM precipitation radar, Romatschke et al. (2010) found that different types of organised convection have differing diurnal cycles: deep convective cores peak at about 1700 LT, wide convective cores peak at either 1700-1800 LT or 0300-0400 LT, and broad stratiform regions have a weak diurnal cycle that peaks at about 0600 LT. Romatschke and Houze Jr (2011) investigated this further over the Central Himalayan foothills, concluding that small and medium sized (<44000km²) convective systems develop as monsoon flow is forced upslope, concluding that medium-sized systems were triggered at lower elevations by katabatic flow.

1.3 | Aims and outline

In this paper, we intend to disentangle the bimodal structure of the diurnal cycle over the Central Himalaya, to quantify the respective roles of katabatic and convective processes, to understand how these processes interact with each

82 other, and whether forcing from large-scale modes of intraseasonal variability offers additional predictability for rainfall
 83 over the Central Himalaya.

84 We outline the data and methods used in Sec. 2. The results are discussed in Sec. 3: the diurnal cycle is inves-
 85 tigated and decomposed in Sec. 3.1, the synoptic-scale elements associated with each component are explored in
 86 Sec. 3.2, and responsible modes of intraseasonal variability are discussed in Sec. 3.3. Finally we discuss the implica-
 87 tions of our results in Sec. 4 and conclude in Sec. 5.

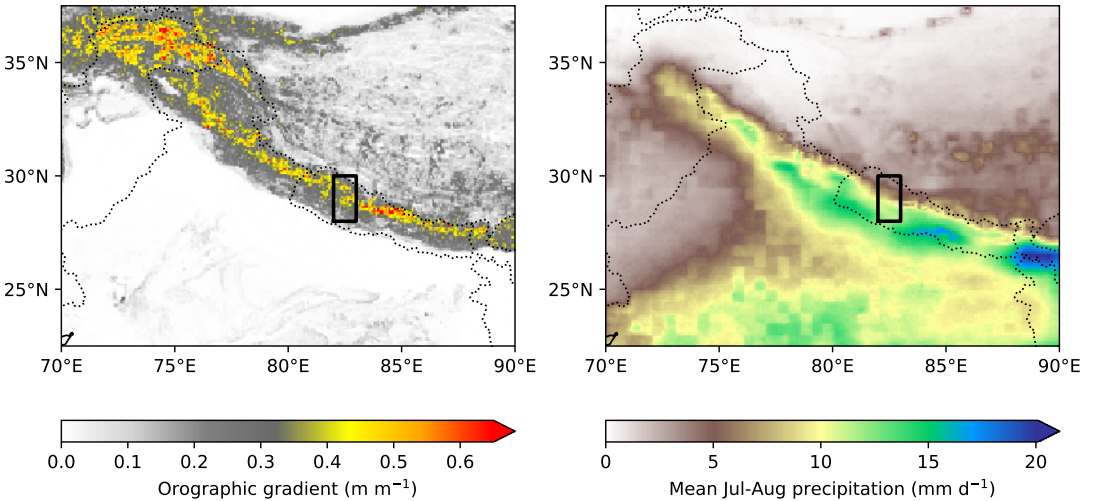


FIGURE 1 The environment of the Central Himalayan foothills. (a) Orographic gradient (m m^{-1}) computed using ETOPO1, downscaled to 8 km using a maximum filter. (b) Mean July–August precipitation (mm d^{-1}) computed using GPM-IMERG data (2000–2019). In each panel, the study region is marked by a black rectangle.

88 2 | DATA AND METHODS

89 2.1 | Data

90 2.1.1 | GPM-IMERG

91 For our precipitation dataset, we use the gridded surface product Integrated Multi-Satellite Retrievals for GPM (IMERG;
 92 Huffman et al., 2015). This has global coverage at a half-hourly, 0.1° resolution, starting June 2000 and continuing to
 93 the present day. Over the tropics, IMERG primarily ingests retrievals from (for 2000-2014) the now-defunct Tropical
 94 Rainfall Measuring Mission (TRMM; Kummerow et al., 1998, 2000) 13.8 GHz precipitation radar and microwave im-
 95 ager (Kozu et al., 2001) and (for 2014-) the Global Precipitation Measurement (GPM; Hou et al., 2014) Ka/Ku-band
 96 dual-frequency precipitation radar. When an overpass is not available, precipitation is estimated by calibrating infrared
 97 measurements from geostationary satellites. While GPM-IMERG performs well when compared against gauge-based
 98 products, performance falls at higher elevations or when quantifying extreme rainfall events (Prakash et al., 2018),
 99 although it performs well over the Western Himalaya (Baudouin et al., 2020). IMERG has good skill in capturing the
 100 diurnal cycle over tropics and subtropics; e.g. for Africa (Dezfuli et al., 2017) and China (Tang et al., 2020).

101 2.1.2 | CMORPH

102 CMORPH (Joyce et al., 2004) is also a multi-satellite precipitation dataset, though unlike GPM-IMERG it does not
103 undergo a gauge calibration adjustment process. It is available at hourly, $0.1^\circ \times 0.1^\circ$ resolution from 2000 onwards. We
104 use CMORPH as an alternative to GPM-IMERG to replicate results and quantify uncertainty. Data were downloaded
105 from ftp://ftp.cpc.ncep.noaa.gov/precip/global_CMORPH/3-hourly_025deg/.

106 2.1.3 | Kalpana OLR

107 To identify regions of deep convection, we use gridded OLR derived from the very-high resolution radiometer onboard
108 the Kalpana satellite (Mahakur et al., 2013; Singh et al., 2007). The data are available from 2004–2017 at three-
109 hourly, $0.25^\circ \times 0.25^\circ$ resolution from 40°S – 40°N and 25°E – 125°E . Data are curated by the Indian Institute of Tropical
110 Meteorology and were downloaded from [https://www.tropmet.res.in/~mahakur/Public_Data/index.php?dir](https://www.tropmet.res.in/~mahakur/Public_Data/index.php?dir=K10LR/3Hrly)
111 [=K10LR/3Hrly](https://www.tropmet.res.in/~mahakur/Public_Data/index.php?dir=K10LR/3Hrly).

112 2.1.4 | ERA5

113 To investigate the local and synoptic-scale structure of the boundary layer and troposphere, we use data from the
114 ECMWF ERA5 reanalysis (Hersbach et al., 2020). Data are available globally, at hourly resolution from 1950 onwards,
115 on a $0.25^\circ \times 0.25^\circ$ grid. Data are available over 37 pressure levels from 1000 to 0.01 hPa, as well as at selected heights
116 above the surface. Data are assimilated into the forecasting system from a large variety of sources, including satellites,
117 automatic weather stations, and radiosondes.

118 2.1.5 | LPS tracks

119 We use the database of low-pressure system (LPS) tracks from Hunt and Fletcher (2019) in this study. Using six-
120 hourly ERA-Interim data, they tracked LPSs by computing the mean relative vorticity in the 900–800 hPa layer, then
121 performing a spectral truncation at T63 to filter out short-wavelength noise. They then identified regions of positive
122 relative vorticity within this field and determined the centroid location for each one. These centroids were then linked
123 in time, subject to constraints in distance and steering winds, to form candidate LPS tracks. This algorithm has been
124 used for monsoon LPSs by a number of authors (e.g. Martin et al., 2020; Dong et al., 2020; Arulalan et al., 2020). Track
125 data are available at <https://doi.org/10.5281/zenodo.5575336>.

126 2.1.6 | BSISO indices

127 Data for the BSISO were downloaded from http://iprc.soest.hawaii.edu/users/kazuyosh/Bimodal_IS0.html,
128 whose methodology is described in Lee et al. (2013). It is used to assess the role of large-scale intraseasonal variability
129 in modulating the diurnal cycle of precipitation over the Himalayas. The dataset has daily resolution, available from
130 1979–2018. It contains the normalised values of the first two principal components (or RMMs), as well as the resulting
131 phase and amplitude.

132 2.2 | Methods

133 We start with the selection of an appropriate study region. The region must be small, so that competing processes
 134 do not smear out the mean diurnal cycle across it. It must also be representative of the rainfall and orography across
 135 the Central Himalaya (i.e. avoiding extremes in either). To this end, we selected 82–83°E, 28–30°N as our study
 136 region (see Fig. 1). Unless stated otherwise, throughout the manuscript, averages and climatologies are computed for
 137 July and August, when the monsoon fully covers the Himalaya. We use UTC and local time (LT, equivalent to Indian
 138 Standard Time; UTC+5:30) in parallel throughout the study to aid the reader while maintaining a standardised time
 139 format. Where phrases such as ‘morning’, or ‘late afternoon’ are used, this always refers to the local time.

140 2.2.1 | Circular standard deviation

141 When dealing with angular data (such as hours of the day), the conventional standard deviation is inadequate as it
 142 does not appropriately handle the discontinuity at 2π . To compute the circular, or ‘directional’ standard deviation, we
 143 use the following calculation (Fisher, 1995) for a one-dimensional series a with cycles of length Ω :

$$S = \frac{1}{n} \sum_1^n \sin\left(\frac{2\pi}{\Omega} a_n\right); C = \frac{1}{n} \sum_1^n \cos\left(\frac{2\pi}{\Omega} a_n\right), \quad (1)$$

144 then the circular variance, R , is given by:

$$R = \sqrt{S^2 + C^2}, \quad (2)$$

145 and hence the circular standard deviation, σ_c :

$$\Omega \cdot \sqrt{-2 \log R}. \quad (3)$$

146 For the diurnal cycle, $\Omega = 24$ hours.

147 2.2.2 | Choice of study region

148 This study is concerned with the diurnal cycle along the foothills and Himalaya. However, this is a broad region and
 149 the synoptic conditions in the western Himalaya are often very different from those in the east. We therefore select a
 150 representative study region, over which the dynamics will be locally coherent, but which can still capture the range of
 151 processes potentially governing the diurnal cycle in both the foothills and the Himalaya. To this end, using data shown
 152 in Fig. 1 we choose the box [82–83°E, 28–30°N]. This is in the Central Himalaya, which feels the full force of the
 153 summer monsoon between July and August, and contains surface elevations ranging from ~500 m in its southwest
 154 to over 5000 m in its northeast, and has a footprint much smaller than the typical length scale of the synoptic-scale
 155 dynamics that typically dominate the region. It also has no significant valleys or bodies of water, but captures the
 156 band of steep orographic gradient that stretches along the Central Himalaya.

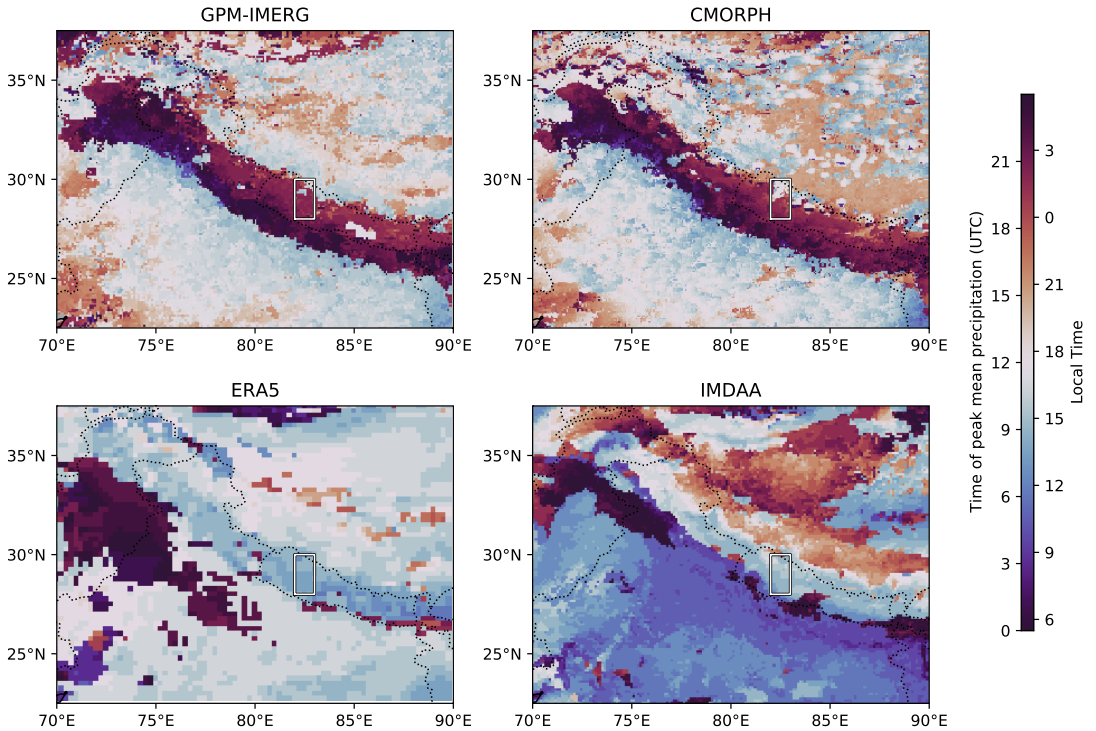
157 **3 | RESULTS**158 **3.1 | Disentangling the diurnal cycle**

FIGURE 2 Time of the peak of the mean diurnal cycle of July–August precipitation over the Himalayas computed for selected datasets. Top: GPM-IMERG and CMORPH are primarily satellite-based products. Bottom: ERA5 and IMDAA are high-resolution reanalyses with parameterised convection. The study region is marked by a white rectangle.

159 We start by quantifying the diurnal cycle in a range of satellite and reanalysis products before using composite
 160 synoptic charts and vertical cross sections to quantify the underlying processes.

161 An overview of the diurnal cycle of monsoon precipitation in two satellite products (GPM-IMERG and CMORPH)
 162 and two reanalysis products (ERA5 and IMDAA) is given in Fig. 2. Here, the peak time of the diurnal cycle is computed
 163 by creating the mean diurnal cycle of July–August precipitation at each pixel in each dataset and then identifying the
 164 time of the maximum value of that cycle. The two satellite products bear a strong similarity and highlight several key
 165 features. First, along the region of steepest orographic gradient (from the foothills to the peaks), stretching from the
 166 east to the west Himalaya, the peak precipitation occurs predominantly during early local morning (~21 UTC, or 03
 167 LT). Within this ‘foothill’ band is a slight meridional gradient, such that the peak precipitation at its southern boundary
 168 occurs 1–2 hours later than at the northern boundary. The foothill band is also punctuated, particularly in GPM-
 169 IMERG, by smaller regions where the peak precipitation occurs in the local late afternoon (~12 UTC, or 18 LT), which
 170 are collocated with larger valleys embedded within the foothills. To the south of the foothills lies the Indo-Gangetic

171 Plain, for which both satellite datasets agree that the peak monsoon rainfall occurs in the local mid-afternoon (~09
 172 UTC, or 15 LT), about twelve hours apart from the peak activity in the foothills. This is consistent with the diurnal
 173 cycle of tropical convection, and varies little in this region, although both GPM-IMERG and CMORPH agree that it
 174 occurs a little earlier in the north and up to a few hours later towards the southwest (Gujarat). Finally, north of the
 175 foothills and the Himalaya, lies the Tibetan Plateau. This is a region of comparatively low precipitation and the satellite
 176 datasets disagree here more than in any other region, although both suggest that precipitation peaks generally in local
 177 mid or late afternoon.

178 The two reanalyses show a mixed ability to capture this regional variability. Over the plains, both ERA5 and
 179 IMDAA put the diurnal peak, correctly, in the mid-to-late local afternoon. However, ERA5 does not capture the
 180 subtle meridional gradient, and IMDAA is several hours too early. Regardless, this is a significant improvement over
 181 earlier reanalyses, whose parameterisation schemes tended to prefer triggering tropical convection at local noon (Dai
 182 and Trenberth, 2004; Dirmeyer et al., 2012). The reanalyses both appear to extend the tropical convection signal
 183 northward over the foothills, placing a mid-afternoon peak along much of the region, at odds with the two satellite-
 184 based datasets. Early morning peaks are only present, for both reanalyses, towards the far northwest and at small,
 185 isolated locations along the very southern boundary. It is interesting that despite having different underlying models
 186 – ERA5 uses the ECMWF IFS and IMDAA uses the Met Office Unified Model – and assimilating different data, the
 187 two reanalyses suffer similar errors along the foothills. In the western Himalaya, where monsoon precipitation is weak
 188 (see Fig. 1), this error can be explained by the tendency of the models to produce too much convective precipitation
 189 or advect it too far north. This bias would likely disappear should the nocturnal dynamics cause the observed early
 190 morning peak to take over. Over the Tibetan Plateau, ERA5 captures the broad mid-to-late afternoon peak, but
 191 IMDAA has significant difficulty, tending to place rainfall around local midnight, but with a large spatial variability.
 192 Model precipitation here is typically produced by the underlying large-scale microphysics schemes (Sharma et al.,
 193 2021), and so is probably not related to IMDAA's convective scheme, rather the fact that it assimilates substantially
 194 fewer observations from outside India (Rani et al., 2021).

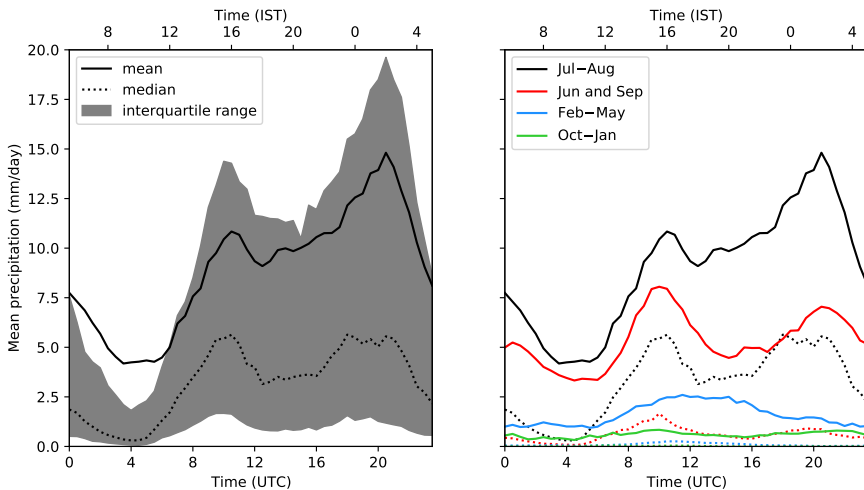


FIGURE 3 The diurnal cycle of precipitation over the study region (82–83°E, 28–30°N). Left: the mean (solid black), median (dotted black), and interquartile range (grey) of the diurnal cycle in July and August. Right: the mean (solid) and median (dotted) diurnal cycles for selected seasons. Computed using GPM-IMERG data from 2000–2020.

195 Figure 3 shows some characteristics of the diurnal cycle over the study region (82–83°E, 28–30°N; see Sec. 2.2.2).
196 Precipitation here is not marked by a single nocturnal peak, but instead by two distinct peaks: one in mid-afternoon
197 centred at 09–10 UTC (15–16 LT) and a larger one just after local midnight centred at 20–21 UTC (02–03 LT). This
198 suggests a greater complexity to the processes underlying the diurnal cycle than analysis of the satellite data in Fig. 2
199 first suggested – although the nature of the reanalysis errors hinted that more than one mechanism may be at play.
200 The peaks have approximately equal magnitude when the median diurnal cycle is considered, implying a longer tail
201 in the nocturnal distribution (i.e., populated by comparatively heavier rainfall events). Both peaks are broad, as well,
202 suggesting that either the rainfall events involved have a reasonable duration, and/or that the timing of the trigger
203 mechanisms can vary from day to day.

204 The diurnal cycle changes throughout the year, as well. When the monsoon is undergoing onset or withdrawal
205 (June and September), it is considerably less active over the Himalaya. During this period, the earlier, mid-afternoon
206 peak has a higher mean than the nocturnal peak – indicating that the underlying mechanisms respond differently to the
207 cloudiness and moisture brought by the presence of an active monsoon trough – the northern edge of which can often
208 reach the foothills. The post-monsoon season (October to January) has a very similar pattern to June and September,
209 though with a much smaller magnitude. In contrast, the pre-monsoon season (Feb–May), has an altogether different
210 diurnal cycle: it is unimodal, with a much broader peak around the late afternoon and early evening. Precipitation
211 during these months is typically brought by isolated convective events that take longer to build up than during the
212 monsoon due to the more stable, drier atmosphere (Shrestha et al., 2012).

213 To start to untangle the processes responsible for these peaks, and their variability, we look at composite daily
214 data, split according to the timing of peak precipitation. We do this for anomalous rainfall over north India and the sur-
215 rounding region in Fig. 4. These composites are constructed thus: mean daily precipitation (00–00 UTC) is computed
216 over the study region for days in July and August during the available GPM-IMERG period (2000–2020). Days with
217 precipitation in the lowest quartile are then separated, and labelled in Fig. 4 as ‘weak rain’. Remaining days are then
218 categorised according to the timing of peak precipitation in the study region, binned into three-hourly groups, and
219 composited. Anomalies are computed relative to the mean of days not included in ‘weak rain’. For each composite,
220 the mean diurnal cycle in the study region is also given. These composite diurnal cycles each have a distinct, unimodal
221 peak, varying in magnitude between 1 and 2 mm hr⁻¹, and contributions from events not associated with the main
222 peak are largely reduced (see, for example, the suppressed nocturnal precipitation in the 09–12 UTC composite). As-
223 sociated rainfall anomalies have a footprint much larger than the study region itself, often spanning several hundred
224 kilometres. Combined with the presence of distinct peaks, this implies that day-to-day variability of larger-scale con-
225 ditions is responsible for modulating the timing of the diurnal cycle, even if the driving mechanisms themselves are
226 localised. Using the structure of the rainfall anomalies, we can start to speculate on what these sources of variability
227 might be, as the spatial scale is consistent with an active BSISO, monsoon trough, or monsoon LPS.

228 3.2 | Synoptic-scale drivers

229 To explore these structures in more detail, we extract days associated with the two diurnal peaks and construct
230 vertical-meridional cross-section composites through the middle of the study region (82.5°E) but extending further
231 north (32.5°N) and south (22.5°N). Fig. 5 shows this for days in which the diurnal peak occurs between 06 and 09
232 UTC, and between 18 and 21 UTC. The anomalies for each field are computed relative to the daily mean for each
233 subset – that is, the sum of the four panels in each of (a) and (b) is zero. The two sets of days share many common
234 features: the diurnal cycle of solar heating and radiative cooling of the surface and boundary layer results in a pair of
235 counterflowing jets in the valley between the foothills and the Deccan Plateau that semidiurnally reverse direction,

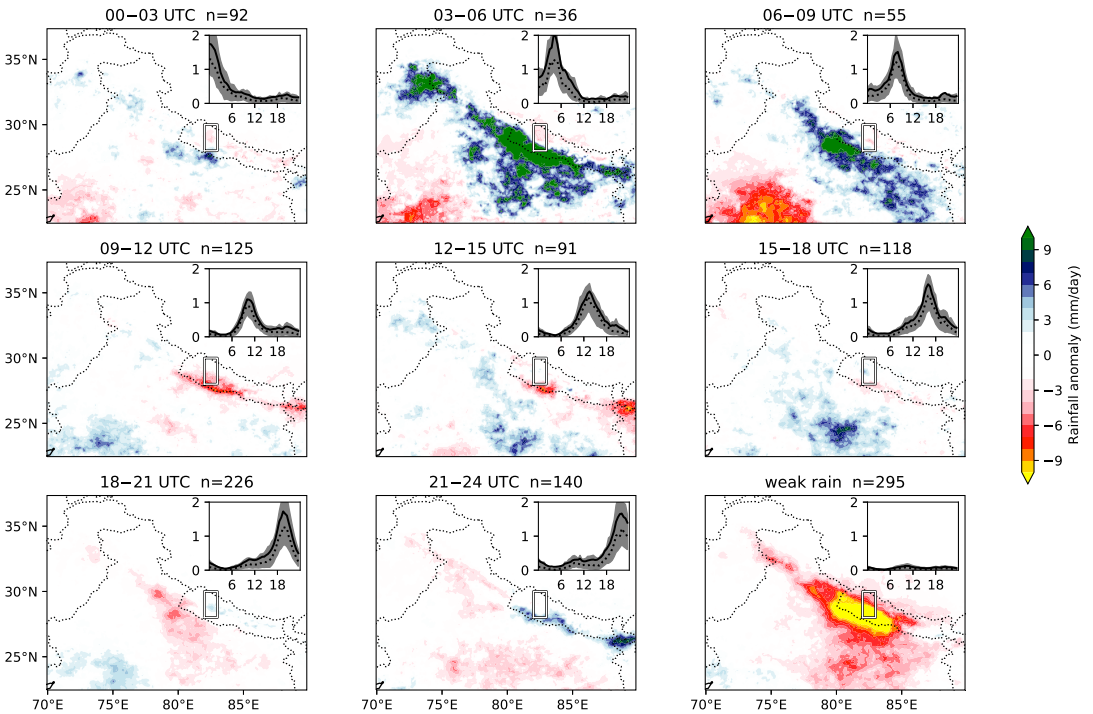


FIGURE 4 Composite anomalous daily rainfall, stratified by the timing of the peak of the diurnal cycle in the study region (marked by a white rectangle). Inset are the mean (black line), median (dotted line) and interquartile range (grey) of the composite UTC diurnal cycles of precipitation (mm hr^{-1}) for each subset, computed over the study region. The number of days included in each composite is given in the panel title, with 'weak rain' days - those on which the mean rainfall within the study region is below the 25th percentile - are considered separately. Uses GPM-IMERG data from July and August 2000–2020. The study region is marked by a white rectangle.

236 consistent with numerical predictions (de Wekker et al., 1998). The most significant difference between the two
 237 sets of days is the timing of ascending moisture flux on the slopes. At the peak, ascent is strongly tied to diurnal
 238 heating with the maximum occurring consistently at 12 UTC; however, further downslope, over our study region,
 239 the maximum upward vertical moisture flux occurs near to, or slightly before, the time of maximum rainfall. This is
 240 perhaps surprising given the reanalysis still prefers nocturnal rainfall, even on days in which late afternoon precipitation
 241 is observed. The strong ascent at 06 UTC in Fig. 5(a) is supported by continued surface heating through 12 UTC.
 242 The boundary layer subsequently cools (18 UTC), either through evaporative cooling by precipitation or increased
 243 cloud cover. Either way, this results in increased stratification and a more stable lower troposphere along the slopes,
 244 suppressing any later nocturnal rainfall. This may explain why days on which afternoon precipitation occurs over the
 245 study region do not then continue to rain the following early morning, which is supported by the behaviour of ERA5
 246 precipitation in Fig. 5(b), where a positive bias in afternoon precipitation comes at the cost of a negative bias in early
 247 morning precipitation. A brief caveat here: these composites use pressure level data, and so near-surface katabatic
 248 and anabatic winds and related density currents may not be appropriately represented. This will be addressed later.

249 This inspection of the diurnal cycle is informative, but does not offer much to help us understand the large-
 250 scale differences in atmospheric conditions that drive the competing mechanisms. So, in Fig. 6, which otherwise has

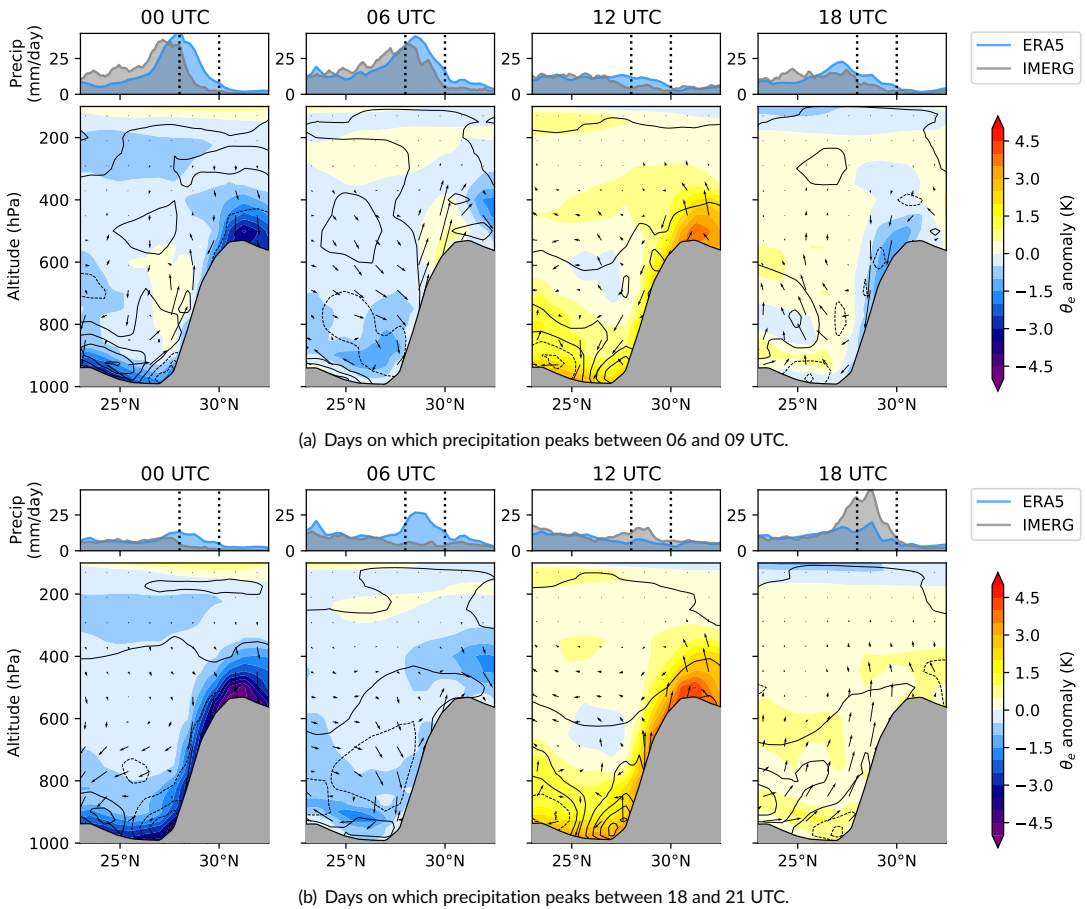


FIGURE 5 Diurnal cycle of selected instantaneous variables, shown as a cross-section through 82.5°E for days on which peak precipitation in the study region occurred (a) between 06 and 09 UTC (1130 and 1430 LT), and (b) between 18 and 21 UTC (2330 and 0230 LT). Meridional-vertical cross-sections show anomalous equivalent potential temperature (coloured contours, K), anomalous moisture flux normal to the cross-sectional plane (line contours in intervals of 5 g kg m s^{-1} , solid lines indicate westerly flow, dashed lines easterly) and anomalous moisture flux parallel to the cross-sectional plane (arrows, vertical exaggerated $200\times$). Anomalies are computed relative to the daily mean. Above each panel, on the same meridional axis, mean precipitation rate (ERA5: blue, GPM-IMERG: grey) over the next six hours (e.g. over 00-06 UTC in the first panel) is plotted.

251 identical construction to Fig. 5, we take the anomalies relative to the time of day over the full Jul–Aug climatology.
 252 For example, fields plotted at 12 UTC have the 12 UTC climatology subtracted from them, which has the effect of
 253 removing the mean diurnal cycle. In this way, we can draw out the differences between the two subsets without the
 254 signal being swamped by diurnal variability.

255 The most striking difference between the two sets of cycles is the presence of a low-level jet. This is distinct from
 256 the nocturnal jet in Fig. 5, and its scale is indicative of synoptic, rather than local, forcing. This anomalous moisture
 257 flux is centered at around 900 hPa, but extends up through to the mid-troposphere, it is easterly for days with peak
 258 precipitation between 06 and 09 UTC (1130 and 1430 LT) and westerly for days with peak precipitation between

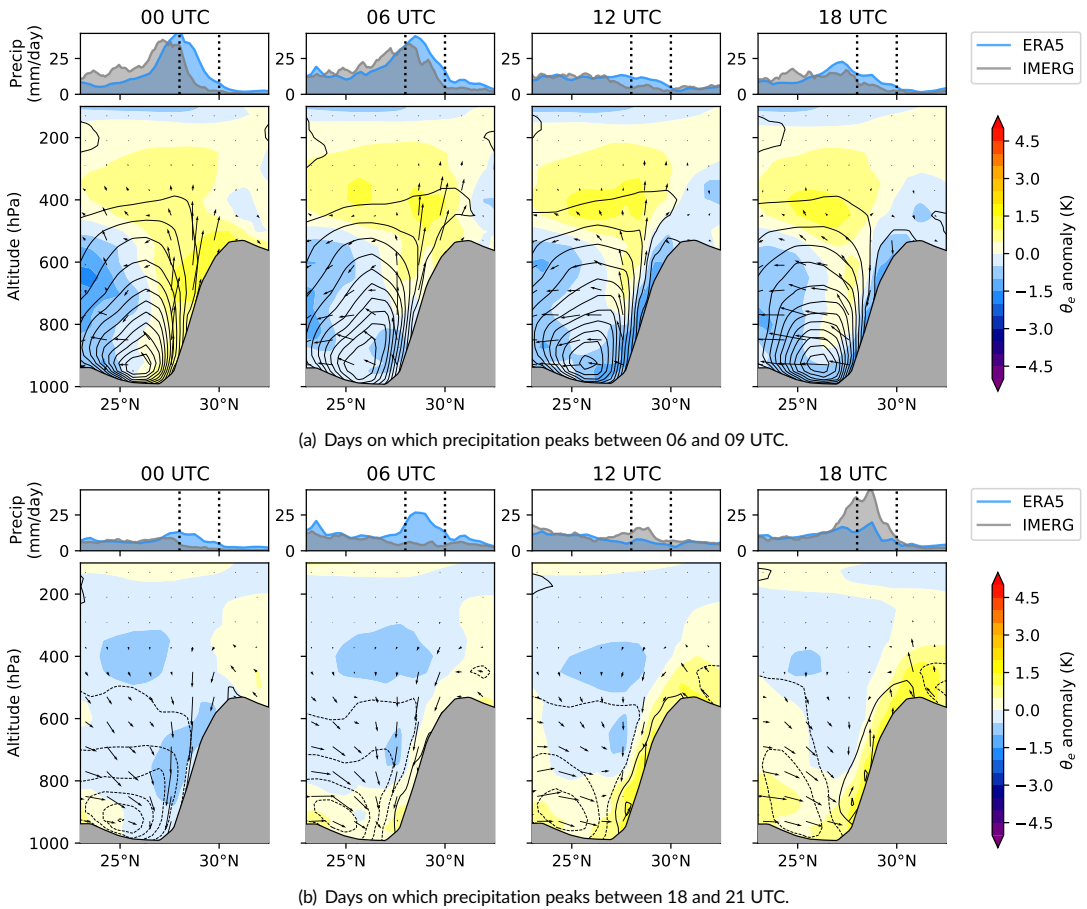


FIGURE 6 As Fig. 5 except anomalies are computed relative to the same time of day over all days. For example, the 18 UTC composite is shown as an anomaly to the 18 UTC Jul-Aug mean.

259 18 and 21 UTC (2330 and 0230 LT). This pattern extends over the whole set of peaks: days with peak precipitation
 260 between 09 and 21 UTC (1430 and 0230 LT) are associated with easterly anomalous moisture flux south of the
 261 foothills, whereas days with peak precipitation between 21 and 09 UTC (0230 and 1430 LT) are associated with
 262 westerly moisture flux. There is a thermal response to, and hence secondary circulation associated with, this jet. For
 263 example, the anomalous westerly jet present on days with daytime peaks is balanced by a positive meridional gradient
 264 in θ_e , the secondary circulation thus provides moisture and updrafts to the foothills, supporting the usual diurnal cycle
 265 of tropical convection (peaking during the local afternoon). In contrast, the easterly jet is associated with large-scale
 266 downdrafts over the region, suppressing canonical tropical convection and generally supporting nocturnal katabatic
 267 flow.

268 To explore the synoptic-scale conditions responsible for supporting these anomalous jets, we partition days ac-
 269 cording to Fig. 3: those with peak precipitation between 18 and 06 UTC (i.e. midnight to midday local time) are
 270 considered 'nocturnal' peak days, and those with peak precipitation between 06 and 18 UTC (i.e. midday to midnight
 271 local time) are considered 'daytime' peak days. Compositing 12 UTC (0530 LT) vertical wind speed and 750 hPa winds

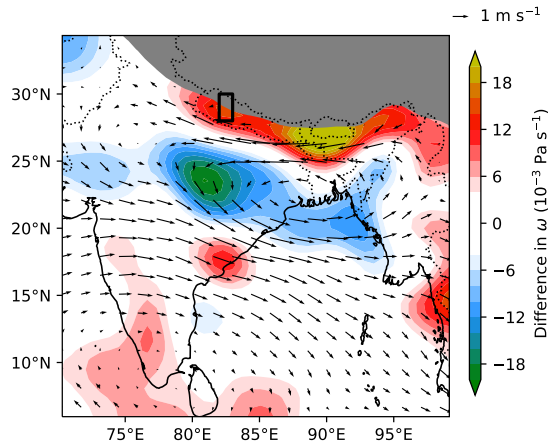


FIGURE 7 Difference between composite daily mean 750 hPa horizontal winds (arrows) and vertical wind speed (coloured contours) on days in which peak precipitation in the study region occurs between 18 and 06 UTC (2330 and 1130 LT) and days in which it occurs between 06 and 18 UTC (1130 and 2330 LT). Areas where climatological surface pressure is less than 750 hPa are greyed out. Negative values of ω indicate ascent. The study region is marked with a black rectangle.

272 for each and taking the difference (Fig. 7) shows that the two groups are associated with significantly different monsoon conditions. Nocturnal peak days are associated with a deepening of the monsoon trough, increased ascent over
 273 the head of the Bay of Bengal and monsoon core zone, and reduced ascent (or increased descent) along the foothills due to barrier flow effects – consistent with Fig. 6(b). The reverse is true for daytime peak days: an anomalously
 274 weak trough allows synoptic-scale anomalous westerlies to impinge on the Himalaya, with the subsequent forced ascent supporting large-scale deep convection. The composite difference of these synoptic conditions is consistent
 275 due to barrier flow effects – consistent with Fig. 6(b). The reverse is true for daytime peak days: an anomalously
 276 weak trough allows synoptic-scale anomalous westerlies to impinge on the Himalaya, with the subsequent forced ascent supporting large-scale deep convection. The composite difference of these synoptic conditions is consistent
 277 ascent supporting large-scale deep convection. The composite difference of these synoptic conditions is consistent
 278 with either an active spell of the monsoon or the passage of a monsoon low-pressure system. We will explore this
 279 hypothesis further in Sec. 3.3.

280 To complete our understanding of the diurnal cycle, we must ask how these two driving processes – deep convec-
 281 tion supported by synoptic-scale flow, and the more localised katabatic flow – project onto it. Are they actually cou-
 282 pled to the cycle, and does this coupling change meaningfully between days with different precipitation peak timing?
 283 We can explore these relationships in detail by examining the phase space of the composite diurnal cycle for different
 284 sets of days. Figure 8 shows the mean diurnal cycles of 10-m v (a proxy for katabatic flow), vertically-integrated mois-
 285 ture flux convergence (VIMFC; a proxy for large-scale deep convection), and precipitation, averaged over the study
 286 area. Two sets of days are included, representing the two local peaks in Fig. 3: those with peak precipitation occurring
 287 between 06 and 09 UTC, and those occurring between 18 and 21 UTC.

288 The two sets of days present markedly different composite diurnal cycles in this phase space. On the daytime
 289 peak days (06–09 UTC), mean VIMFC peaks at $3.6 \times 10^{-4} \text{ kg m}^{-2} \text{ s}^{-1}$ at about 08 UTC, remaining high for several
 290 hours. The peak precipitation immediately follows this event. In contrast, on nocturnal peak days (18–21 UTC), the
 291 VIMFC peak is much shorter and weaker, reaching only $2.5 \times 10^{-4} \text{ kg m}^{-2} \text{ s}^{-1}$. This means that much less moisture
 292 is available for deep convection in the afternoon and as a result, very little precipitation occurs at this time. This is
 293 corroborated (not shown) by the composite diurnal cycle of 500 hPa ω .

294 We can also see the relative importance of the low-level cross-slope winds. Climatologically, these are slightly
 295 upslope (positive 10-m v) because of the orientation of the monsoon trough relative to the foothills; however, at

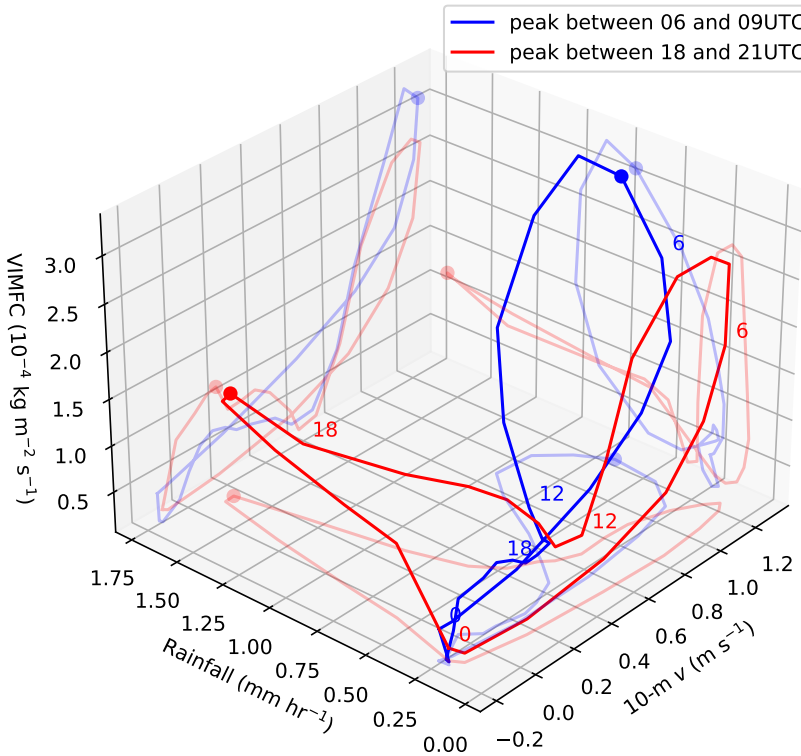


FIGURE 8 Three-dimensional phase space showing the relationship between cross-slope surface flow, vertically integrated moisture flux convergence, and rainfall over the course of the diurnal cycle. Composited for days on which peak precipitation occurs between 06 and 09 UTC (blue) and 18 and 21 UTC (red). Circle markers indicate the mean time of peak precipitation, and additional numerical markers indicate the UTC time of day for each cycle. The pale sets of red and blue lines show the projection of the cycle onto the three respective axis planes.

296 night, as the katabatic effect reaches a maximum, these approach zero or even become negative. Here, the role of the
 297 large-scale is again important: during nocturnal days, peak precipitation occurs as 10-m v approaches its lowest value,
 298 but this also coincides with an increase in VIMFC – suggesting that in such cases the katabatic flow is interacting with
 299 the monsoon environment at the north edge of the trough to produce moisture convergence along the slope. During
 300 daytime peak days, there is no simultaneous increase in VIMFC at this time, and hence no heavy precipitation. So,
 301 while the katabatic and convective processes are the primary drivers for the two sets of peaks, they do not operate
 302 entirely independently. In the same way, we see in Fig. 8 how the convective peak may be further supported by
 303 anabatic winds. These feedbacks are complementary to the mechanism proposed by Barros and Lang (2003), who
 304 found that daytime precipitation over Nepal was favoured during periods where strong anabatic flow prevented the
 305 build up of moisture convergence in the lower foothills.

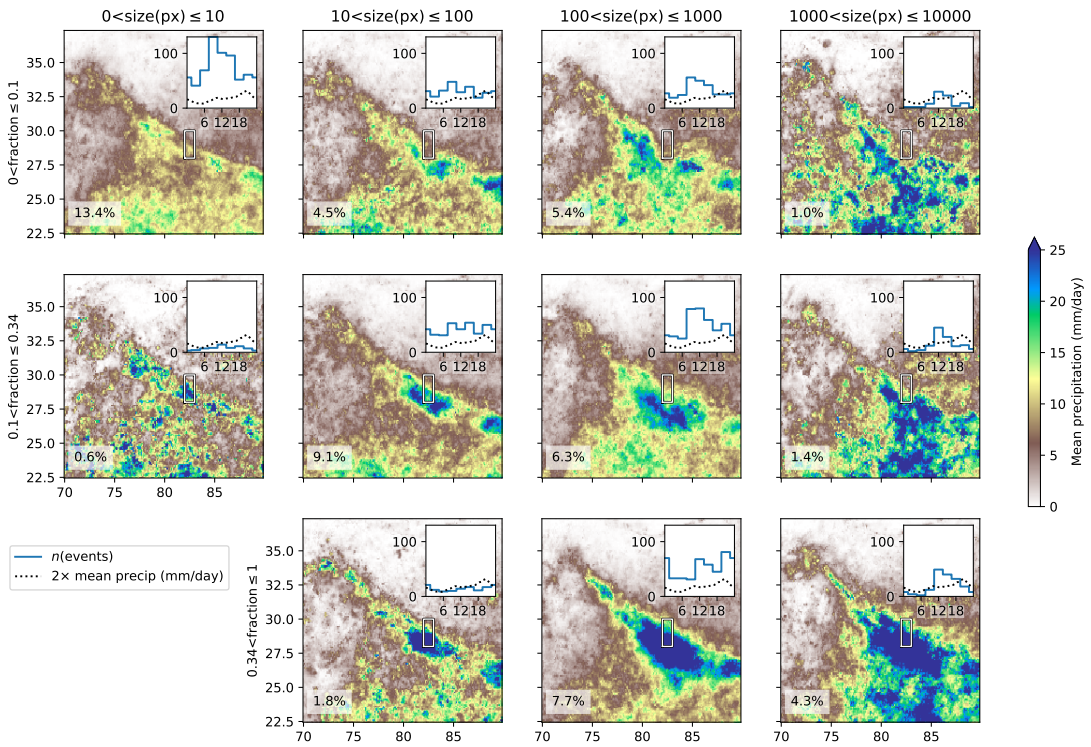


FIGURE 9 The relationship between convective organisation and the diurnal cycle. Convective regions are identified in Kalpana OLR data as contiguous areas with $OLR < 167 \text{ W m}^{-2}$. Convective regions that overlap the study region are then binned according to their area (measured in $0.25^\circ \times 0.25^\circ$ pixels, columns), and fraction of study area covered (rows). Composite mean precipitation is given for each pair of bins, with the diurnal cycle of event frequency inset (blue). Given in the inset, for comparison, is the mean diurnal cycle of precipitation (scaled for clarity) for Jul–Aug. The fraction of total Jul–Aug 06–15 UTC (precipitation that occurs during each subset is given in the lower left of the respective panel).

306 3.3 | Response to intraseasonal forcing

307 3.3.1 | The relationship between convective organisation and the diurnal cycle

308 In the rest of this study, we will dedicate ourselves to understanding the drivers behind the convective processes that
 309 cause precipitation to fall over the Central Himalaya during the local afternoon or early evening. There are several
 310 reasons for this focus. Firstly, as we saw in the introduction, the katabatic processes over this region are generally
 311 well understood. Secondly, daytime precipitation over this region is the exception rather than the rule, and so it is
 312 important to quantify potential sources of variability, particularly given the challenge of simulating the diurnal cycle
 313 of convection in the tropics (Watters et al., 2021).

314 We start by exploring the structure and variability of deep convection itself over the region surrounding the
 315 Central Himalaya. Using Kalpana satellite OLR data, we located contiguous regions of deep convection by identifying
 316 $0.25^\circ \times 0.25^\circ$ pixels where $OLR < 167 \text{ W m}^{-2}$. Regions were then jointly categorised according to their area, and the
 317 fraction of the study region they covered. Composite precipitation for the twelve sets of bins (except for very small
 318 storms covering the whole study region, for which there were no cases) is shown in Fig. 9, along with the diurnal

319 cycle for each type, and the fraction of daytime rainfall for which that category is responsible. The total attributable
320 fraction is 55.5%, and this would likely be higher still if we used a more relaxed threshold for identifying convection,
321 or a higher resolution OLR product capable of resolving isolated deep convection. In contrast, only about 30% of
322 nocturnal precipitation can be explained in this way.

323 Contributions come from a range of different sizes of storm. The smallest ($\leq 6250 \text{ km}^2$; length-scale $\leq 80 \text{ km}$)
324 are associated with 14.0% of afternoon and early evening precipitation (1130 to 2030 LT – i.e., the window when
325 convective peaks are most common) over the study region. They provide heavy precipitation to a small area, and
326 closely follow the typical diurnal cycle of convection, peaking at 11 UTC (1630 LT) and decaying over the next few
327 hours. Medium-sized storms ($6250 < A \leq 62500 \text{ km}^2$; length-scale between $\sim 80 \text{ km}$ and $\sim 250 \text{ km}$) contribute 15.4%
328 of the daytime precipitation. Medium-sized storms that are further south, and thus cover only a small fraction of the
329 box, have a diurnal cycle largely consistent with tropical convection, but those that are further north and cover much
330 more of the region have a much flatter diurnal cycle, suggesting that the convective and katabatic modes are mixed
331 at this scale: although the storms are highly convective, either a subset are being triggered by katabatic flow, or they
332 are being intensified by katabatic convergence once mature.

333 The scale of the storm that the katabatic mode can generate is limited both by the length-scale of the orography
334 and the ability of these storms to aggregate given the available environmental shear. Thus, our category of large storms
335 ($62500 < A \leq 625000 \text{ km}^2$; length-scale between $\sim 250 \text{ km}$ and $\sim 800 \text{ km}$) is quite unlikely to be orographically triggered.
336 These storms account for more daytime precipitation (19.4%) than any other size, and the mean diurnal cycle of their
337 frequency peaks at 11 to 13 UTC (1630 to 1830 LT). This peak occurs a few hours later in storms that are further
338 north (see bottom panel), suggesting that they may have initiated to the south and then propagated into the region.
339 The high coverage subset also has a second peak at 20 UTC (0130 LT) which we hypothesize is due to intensification
340 from low-level moisture flux convergence caused by katabatic flow. The largest category of storm ($> 625000 \text{ km}^2$;
341 length-scale greater than $\sim 800 \text{ km}$) is comparatively rare but still contributes nearly 7% of the daytime precipitation
342 to the region, having a well-defined peak in frequency at 12 UTC (1730 LT). The peak is broadest (i.e. the decay is
343 slowest) for systems covering most of the box, again highlighting the role of local orographically-driven dynamics in
344 supporting large-scale storms that arrive over the region.

345 Our discussion on the footprints of deep convection led to four conclusions: (i) deep convection contributes a
346 majority of daytime precipitation over the Central Himalaya; (ii) regardless of scale, it typically follows the canonical
347 diurnal cycle of tropical convection, peaking at around 12 UTC (1730 LT) except (iii) when propagating northward from
348 the trough, in which case it occurs over the foothills several hours later or (iv) when residual storms are intensified
349 at night through interactions with local orographic dynamics. We saw that the contributed precipitation was roughly
350 equal across the three smaller size bins (15-20%) and a bit less for the largest size (7%). Yet, the synoptic conditions
351 differ considerably between environments favourable for small-scale and large-scale convection. At the smaller end,
352 intraseasonal variability tends to be controlled by the BSISO and monsoon active/break cycles; whereas at the larger
353 end, convection is typically organised by low-pressure systems. We will now quantify the effect of each of these
354 flavours of intraseasonal variability on the diurnal cycle of precipitation over the Central Himalaya.

355 3.3.2 | The BSISO

356 We start with the BSISO, often thought of as the meridionally-propagating component of the MJO, it is associated
357 with northwest–southeast bands of positively or negatively anomalous OLR propagating northward across India and
358 Southeast Asia, with a frequency of 10–60 days (Lee et al., 2013). Like the MJO, the BSISO is defined using the
359 phase relationship between two principal component timeseries, and is thus quantified using both a phase (from 1

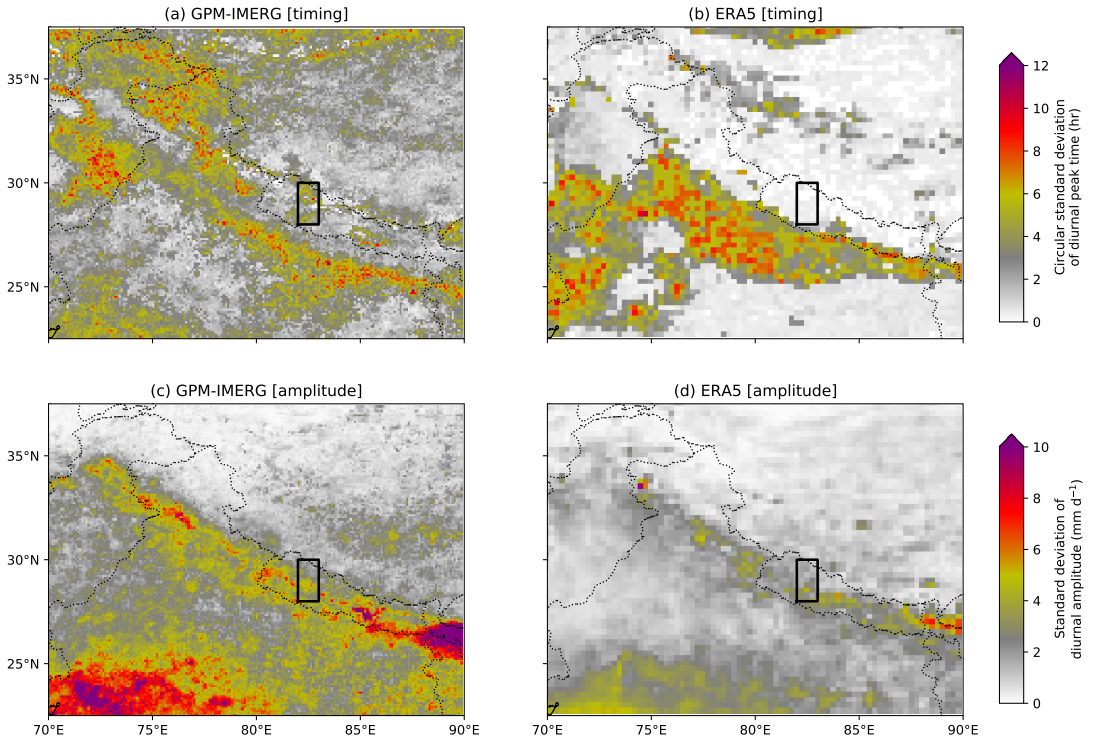


FIGURE 10 Effect of the BSISO on diurnal peak timing (a,b) and amplitude (c,d). The mean diurnal cycle for each BSISO phase is computed at each gridpoint. The circular standard deviation of the peak timing and the standard deviation of the cycle amplitude are then computed. Low values in (a) and (b) suggest the BSISO has little or no impact on the timing of the diurnal peak. The study region is marked with a black rectangle.

360 to 8) and a standardised magnitude. Both the diurnal cycle and the BSISO are ‘circular’ variables in this regard, but
 361 simply computing a direct circular correlation between the two is not appropriate because it relies on the assumption
 362 that the two variables covary somewhat uniformly. This may not be the case: the two peaks on the diurnal cycle,
 363 which are almost opposite in phase, could be strongly associated with neighbouring BSISO phases; but, unless the
 364 relationship with the remaining phases is consistently ordered, the correlation would be low despite plausible causality.
 365 We must take a more nuanced approach. To do this, we compute the mean diurnal cycle for each BSISO phase at
 366 each gridpoint. Then, by taking the standard deviation of the amplitude of those eight cycles, and the circular standard
 367 deviation (see Sec. 2.2.1) of the eight peak times, we can identify regions where the BSISO appreciably affects the
 368 timing and amplitude of the diurnal cycle of precipitation – in regions where the standard deviations are low, the
 369 relationship is weak; where the standard deviation is high, the relationship is strong. To quantify uncertainty, we do
 370 this for both GPM-IMERG and ERA5, the latter of which should capture intraseasonal variability well over the Central
 371 Himalaya, as it does over the Western Himalaya (Baudouin et al., 2020).

372 The BSISO has almost no effect on the timing of the diurnal cycle of ERA5 rainfall over the study region, and
 373 only has a comparatively weak effect on IMERG. There is also only a relatively weak effect on the cycle amplitude:
 374 the magnitude of the convective (10–11 UTC, ~1600 LT) peak averaged over the box only varies from 0.35 to 0.47
 375 mm hr⁻¹ between the different BSISO phases (lowest in phase 4; highest in phase 8). The magnitude of the nocturnal

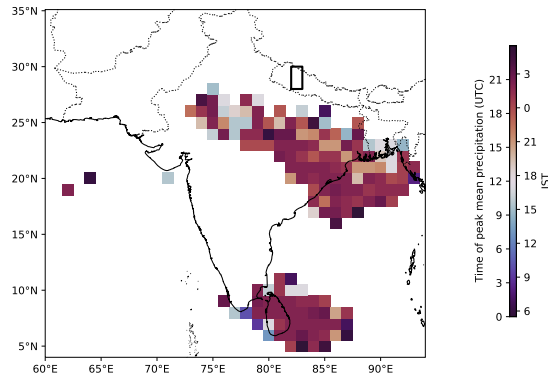


FIGURE 11 The effect of LPS presence on the timing of the diurnal cycle of precipitation over the study region. Track points of LPSs (2000–2018) are binned into a $1^\circ \times 1^\circ$ grid. Gridpoints with at least ten days of LPS overpasses are then coloured according to the peak timing of the mean diurnal cycle over the study region.

376 peak varies between 0.57 and 0.88 mm hr^{-1} (lowest in phase 4; highest in phase 5). These are in broad agreement
 377 with the behaviour of the BSISO, whose negative OLR anomalies reach their furthest north in phase 5, and which
 378 has significant, positive OLR anomalies over the Central Himalaya during phase 4. In summary, while the BSISO can
 379 affect the magnitude of the convective and katabatic peaks to some extent, it is not enough to invert the population
 380 so that the convective peak is stronger than the katabatic peak for any given phase. This may be because the BSISO
 381 does not propagate sufficiently far north: we see that in both IMERG and ERA5 that it does have a substantial effect
 382 on the timing and amplitude of the diurnal cycle further south, over the Indo-Gangetic Plain, a topic that we leave for
 383 further research.

384 3.3.3 | Low-pressure systems

385 Finally, we look at the role of monsoon low-pressure systems (LPSs), which are capable of inducing extended periods
 386 of large-scale moisture flux, organised deep convection, and deepening/extending the monsoon trough. Convective
 387 activity is most sensitive to their location rather than intensity (Hunt et al., 2021), and so in Fig. 11 we bin LPS tracks
 388 onto a $1^\circ \times 1^\circ$ grid and compute the mean diurnal cycle over the study region for the dates included in each box, as
 389 long as at least 10 LPSs were present. When LPSs are either in the centre or the south of the trough, or are located far
 390 away from the Himalaya (e.g. over Sri Lanka or the Arabian Sea), the peak of the mean diurnal cycle remains close to
 391 the katabatic peak at about 21 UTC (0230 LT). Where LPSs are at the northern edge of the trough, or extend it to the
 392 northwest, the convective peak becomes stronger, and the peak of the mean diurnal cycle moves to the afternoon
 393 (09 UTC, 1430 LT), consistent with the larger storm sizes of Fig. 7 and Fig. 9. One possible reason for this is the cloud
 394 structure of LPSs: Hunt et al. (2016) showed that monsoon depressions (their Fig. 5) were often associated with deep
 395 convective cloud near their centre and stratiform cloud at larger radii. Thus, an LPS in the centre of the trough provides
 396 moisture, but not much convective instability to the foothills – supporting the katabatic peak, whereas an LPS further
 397 north may cause deep convective to occur directly over the study region. Further work is needed to explore how LPSs
 398 interact with the orography over the Central Himalaya.

399 4 | DISCUSSION

400 Before concluding, we will briefly discuss some of the caveats and implications of this work in a modelling framework.
401 Perhaps the most important caveat is basing many of our results on the interpretation of reanalysis data. At a horizontal
402 resolution of ~ 25 km, many of the valleys that may be providing the more intense katabatic flow are not represented.
403 Fig. 12 shows the mean diurnal cycle and frequency of peak timing over the study region for GPM-IMERG, ERA5,
404 and two simulations of the 2016 monsoon season in the Met Office Unified Model (MetUM) at horizontal resolutions
405 of 17 km (parameterised convection) and 4.4 km (explicit convection) conducted as part of the INCOMPASS project
406 (Turner et al., 2020). We also include another reanalysis, IMDAA (Rani et al., 2021), which has higher horizontal
407 resolution (12 km) than ERA5, and uses a version of the MetUM as its driving model. To confirm that the statistics
408 for a single season are valid, both the climatology (dotted) and the 2016 season (solid) are plotted for the reanalyses
409 and satellite data. In the reanalyses and 17 km MetUM experiment, we can also partition the rainfall into ‘convective’
410 (produced by the convection scheme) and ‘stratiform’ (produced by the microphysics scheme).

411 Both reanalyses and the 17 km experiment capture the convective and katabatic peaks, but overestimate the
412 magnitude of the convective peak and significantly underestimate the magnitude of the katabatic peak. The coarsest
413 model (ERA5) underestimates this peak the most, and the highest-resolution model (IMDAA) the least, which may
414 imply that fine representation of orography is crucial to correct representation of the katabatic winds (and thus to
415 the nocturnal moisture convergence required for the precipitation). Moisture not used up as precipitation during the
416 katabatic peak is then available later for the convective peak. It is a helpful sanity check to see that the contribution of
417 convective rainfall is much larger during the convective peak than the katabatic peak, where stratiform rainfall plays
418 a more significant role, even overtaking the convective contribution in ERA5. Understanding the respective strengths
419 (e.g. both peaks present and at approximately the right time) and weaknesses (e.g. the relative strengths of the peaks
420 are inconsistent with observation) of these parameterised-convection models is left for future work. The convection-
421 permitting 4.4 km experiment is beset by a different problem. The convection takes too long to build up during the
422 day, since uplifting an entire 4.4 km gridbox requires a lot of instability. This means that the convective peak occurs so
423 late that it interferes with the katabatic peak, resulting in a mean cycle with a single peak in the late evening (2000 LT).
424 This demonstrates that the problem of correctly representing the complex and interacting processes that drive the
425 diurnal cycle here is not simply a matter of increasing resolution. It is likely that this would be improved by models with
426 sub-kilometre resolution (e.g. Yashiro et al., 2016), where convection is resolved rather than just permitted, and where
427 the representation of the orography is fine enough to capture the valleys responsible for strong pulses of katabatic
428 flow, but we leave such an assessment for future work.

429 5 | CONCLUSIONS

430 In this study, we have explored the complex diurnal cycle of precipitation over the monsoonal Central Himalaya. Using
431 a small study region that we believe to be representative ($82\text{--}83^\circ\text{E}$, $28\text{--}30^\circ\text{N}$), we showed that the mean diurnal cycle
432 has two broad peaks, one during the late afternoon (1700 LT) and one during the early morning (0200 LT). The early
433 morning peak has the greater magnitude in the mean cycle during July and August, but this pattern reverses during
434 the pre- and post-monsoon months of June and September, when the late afternoon peak has the greater magnitude.

435 Reanalyses and a 17 km model with parameterised convection broadly capture both peaks, but overestimate the
436 magnitude of the afternoon peak while underestimating the magnitude of the early morning peak. Simple diagnostics
437 that just compute the timing of the maximum of the mean diurnal cycle are thus insufficient to validate model per-

438 formance in this region – simply comparing the peak times of the climatological mean diurnal cycles would point to a
439 phase bias of about 10 hours here, which is an incomplete and exaggerated description of the actual biases.

440 We showed that this bimodal cycle is an artefact of compositing: individual days are usually associated with a
441 single peak that typically lasts for several hours and may occur at any time, although are most frequent during the early
442 morning and late afternoon. Both peaks are associated with a significant low-level nocturnal jet, which can therefore
443 be ruled out as a significant moisture source that preferentially supports one or the other.

444 We confirmed previous studies that showed that the early morning peak was due to katabatic winds interacting
445 with the mean monsoon flow to drive moisture flux convergence along the foothills. We hypothesize that this explains
446 why this peak is comparatively weaker outside the monsoon, and that underestimating the magnitude of the katabatic
447 wind due to coarse orographic representation is a potential source of the bias in models and reanalyses.

448 We showed that the late-afternoon peak is linked to the canonical diurnal cycle of tropical convection, and that
449 the responsible convection occurs at a range of scales ranging from tens (small mesoscale convective systems) to
450 thousands (monsoon low-pressure systems) of kilometres. We found that systems present after midnight could be
451 further intensified at low altitudes by katabatic flow. We hypothesize that anabatic flow may assist in intensifying or
452 triggering convection at higher altitudes during the daytime.

453 We explored a range of sources of intraseasonal variability, finding only very weak relationships between the
454 BSISO and the diurnal cycle, and between the monsoon active/break phases and the diurnal cycle. We also found,
455 however, that monsoon LPSs, when sufficiently far north or west, were capable of significantly intensifying the con-
456 vective peak.

457 Acknowledgements

458 KMRH, AGT, and RKHS are funded through the Weather and Climate Science for Service Partnership (WCSSP) India,
459 a collaborative initiative between the Met Office, supported by the UK Government's Newton Fund, and the Indian
460 Ministry of Earth Sciences (MoES). RKHS is also supported by the

461 references

- 462 Arulalan, T., AchutaRao, K., Hunt, K. M. R., Turner, A. G., Mitra, A. K. and Sarkar, A. (2020) Prediction of western disturbances
463 tracks using NEPS. URL: https://www.ncmrwf.gov.in/event/emmda/Abstracts/TArulalan_Abstract_EMMDA.pdf.
- 464 Barros, A. P., Joshi, M., Putkonen, J. and Burbank, D. W. (2000) A study of the 1999 monsoon rainfall in a mountainous region
465 in central Nepal using TRMM products and rain gauge observations. *Geophysical research letters*, **27**, 3683–3686.
- 466 Barros, A. P., Kim, G., Williams, E. and Nesbitt, S. W. (2004) Probing orographic controls in the Himalayas during the monsoon
467 using satellite imagery. *Natural Hazards and Earth System Sciences*, **4**, 29–51.
- 468 Barros, A. P. and Lang, T. J. (2003) Monitoring the monsoon in the Himalayas: Observations in central Nepal, June 2001.
469 *Monthly Weather Review*, **131**, 1408–1427.
- 470 Baudouin, J.-P., Herzog, M. and Petrie, C. A. (2020) Cross-validating precipitation datasets in the Indus River basin. *Hydrology
471 and Earth System Sciences*, **24**, 427–450.
- 472 Bhatt, B. C. and Nakamura, K. (2006) A climatological-dynamical analysis associated with precipitation around the southern
473 part of the Himalayas. *Journal of Geophysical Research: Atmospheres*, **111**.
- 474 Bluestein, H. B. (1993) *Synoptic-dynamic meteorology in midlatitudes. Volume II. Observations and theory of weather systems*.
475 New York, NY (United States); Oxford University Press. P. 392.

- 476 Bollasina, M., Bertolani, L. and Tartari, G. (2002) Meteorological observations at high altitude in the Khumbu Valley, Nepal
477 Himalayas, 1994-1999. *Bulletin of Glaciological Research*, **19**, 1-12.
- 478 Dai, A. and Trenberth, K. E. (2004) The diurnal cycle and its depiction in the Community Climate System Model. *Journal of*
479 *Climate*, **17**, 930-951.
- 480 Dezfuli, A. K., Ichoku, C. M., Huffman, G. J., Mohr, K. I., Selker, J. S., Van De Giesen, N., Hochreutener, R. and Annor, F. O.
481 (2017) Validation of IMERG precipitation in africa. *Journal of Hydrometeorology*, **18**, 2817-2825.
- 482 Dirmeyer, P. A., Cash, B. A., Kinter, J. L., Jung, T., Marx, L., Satoh, M., Stan, C., Tomita, H., Towers, P., Wedi, N. et al. (2012)
483 Simulating the diurnal cycle of rainfall in global climate models: Resolution versus parameterization. *Climate Dynamics*, **39**,
484 399-418.
- 485 Dong, W.-H., Ming, Y. and Ramaswamy, V. (2020) Projected changes in South Asian monsoon low-pressure systems. *J. Climate*.
486 In review.
- 487 Egger, J., Bajrachaya, S., Egger, U., Heinrich, R., Reuder, J., Shayka, P., Wendt, H. and Wirth, V. (2000) Diurnal winds in the
488 Himalayan Kali Gandaki valley. part I: observations. *Monthly Weather Review*, **128**, 1106-1122.
- 489 Fisher, N. I. (1995) *Statistical analysis of circular data*. Cambridge University Press.
- 490 Fitzjarrald, D. R. (1984) Katabatic wind in opposing flow. *Journal of Atmospheric Sciences*, **41**, 1143-1158.
- 491 Hersbach, H., Bell, B., Berrisford, P., Hirahara, S., Horányi, A., Muñoz-Sabater, J., Nicolas, J., Peubey, C., Radu, R., Schepers, D.
492 et al. (2020) The ERA5 global reanalysis. *Quarterly Journal of the Royal Meteorological Society*, **146**, 1999-2049.
- 493 Hou, A. Y., Kakar, R. K., Neeck, S., Azarbarzin, A. A., Kummerow, C. D., Kojima, M., Oki, R., Nakamura, K. and Iguchi, T. (2014)
494 The global precipitation measurement mission. *Bulletin of the American Meteorological Society*, **95**, 701-722.
- 495 Huffman, G. J., Bolvin, D. T., Nelkin, E. J. et al. (2015) Integrated Multi-satellitE Retrievals for GPM (IMERG) technical docu-
496 mentation. *NASA/GSFC Code*, **612**, 2019.
- 497 Hunt, K. M. R. and Fletcher, J. K. (2019) The relationship between Indian monsoon rainfall and low-pressure systems. *Climate*
498 *Dynamics*, **53**, 1-13.
- 499 Hunt, K. M. R., Turner, A. G. and Parker, D. E. (2016) The spatiotemporal structure of precipitation in Indian monsoon depres-
500 sions. *Quart. J. Roy. Meteor. Soc.*, **142**, 3195-3210. URL: <http://dx.doi.org/10.1002/qj.2901>.
- 501 Hunt, K. M. R., Turner, A. G., Stein, T. H. M., Fletcher, J. K. and Schiemann, R. K. H. (2021) Modes of coastal precipitation over
502 southwest india and their relationship with intraseasonal variability. *Quarterly Journal of the Royal Meteorological Society*,
503 **147**, 181-201.
- 504 Joyce, R. J., Janowiak, J. E., Arkin, P. A. and Xie, P. (2004) CMORPH: A method that produces global precipitation estimates
505 from passive microwave and infrared data at high spatial and temporal resolution. *J. Hydrometeor.*, **5**, 487-503.
- 506 Kikuchi, K. and Wang, B. (2008) Diurnal precipitation regimes in the global tropics. *Journal of Climate*, **21**, 2680-2696.
- 507 Kozi, T., Kawanishi, T., Kuroiwa, H., Kojima, M., Oikawa, K., Kumagai, H., Okamoto, K., Okumura, M., Nakatsuka, H. and
508 Nishikawa, K. (2001) Development of precipitation radar onboard the Tropical Rainfall Measuring Mission (TRMM) satellite.
509 *IEEE Trans. Geosci. Rem. Sens.*, **39**, 102-116. URL: <http://dx.doi.org/10.1109/36.898669>.
- 510 Kummerow, C., Barnes, W., Kozi, T., Shiue, J. and Simpson, J. (1998) The Tropical Rainfall Measuring Mission (TRMM) sensor
511 package. *J. Atmos. Oceanic Technol.*, **15**, 809-817. URL: [http://dx.doi.org/10.1175/1520-0426\(1998\)015<0809:TTRMMT>](http://dx.doi.org/10.1175/1520-0426(1998)015<0809:TTRMMT>2.0.CO;2)
512 [2.0.CO;2](http://dx.doi.org/10.1175/1520-0426(1998)015<0809:TTRMMT>2.0.CO;2).
- 513 Kummerow, C., Simpson, J., Thiele, O., Barnes, W., Chang, A. T. C., Stocker, E., Adler, R. F., Hou, A., Kakar, R., Wentz, F.
514 et al. (2000) The status of the Tropical Rainfall Measuring Mission (TRMM) after two years in orbit. *J. Appl. Meteor.*, **39**,
515 1965-1982. URL: [http://dx.doi.org/10.1175/1520-0450\(2001\)040<1965:TSOTTR>2.0.CO;2](http://dx.doi.org/10.1175/1520-0450(2001)040<1965:TSOTTR>2.0.CO;2).

- 516 Lee, J.-Y., Wang, B., Wheeler, M. C., Fu, X., Waliser, D. E. and Kang, I.-S. (2013) Real-time multivariate indices for the boreal
517 summer intraseasonal oscillation over the Asian summer monsoon region. *Climate Dyn.*, **40**, 493–509.
- 518 Mahakur, M., Prabhu, A., Sharma, A. K., Rao, V., Senroy, S., Singh, R. and Goswami, B. N. (2013) A high-resolution outgoing
519 longwave radiation dataset from Kalpana-1 satellite during 2004–2012. *Current Science*, 1124–1133.
- 520 Marsham, J. H., Dixon, N. S., Garcia-Carreras, L., Lister, G. M. S., Parker, D. J., Knippertz, P. and Birch, C. E. (2013) The role of
521 moist convection in the West African monsoon system: Insights from continental-scale convection-permitting simulations.
522 *Geophysical Research Letters*, **40**, 1843–1849.
- 523 Martin, G. M., Brooks, M. E., Johnson, B., Milton, S. F., Webster, S., Jayakumar, A., Mitra, A. K., Rajan, D. and Hunt, K. M. R.
524 (2020) Forecasting the monsoon on daily to seasonal time-scales in support of a field campaign. *Quarterly Journal of the*
525 *Royal Meteorological Society*, **146**, 2906–2927.
- 526 Prakash, S., Mitra, A. K., AghaKouchak, A., Liu, Z., Norouzi, H. and Pai, D. S. (2018) A preliminary assessment of GPM-based
527 multi-satellite precipitation estimates over a monsoon dominated region. *Journal of Hydrology*, **556**, 865–876.
- 528 Rani, S. I., Arulalan, T., George, J. P., Rajagopal, E., Renshaw, R., Maycock, A., Barker, D. M. and Rajeevan, M. (2021) IMDAA:
529 High-resolution satellite-era reanalysis for the Indian monsoon region. *Journal of Climate*, **34**, 5109–5133.
- 530 Romatschke, U. and Houze Jr, R. A. (2011) Characteristics of precipitating convective systems in the south asian monsoon.
531 *Journal of Hydrometeorology*, **12**, 3–26.
- 532 Romatschke, U., Medina, S. and Houze, R. A. (2010) Regional, seasonal, and diurnal variations of extreme convection in the
533 South Asian region. *Journal of Climate*, **23**, 419–439.
- 534 Rütthrich, F., Thies, B., Reudenbach, C. and Bendix, J. (2013) Cloud detection and analysis on the Tibetan Plateau using Me-
535 teosat and CloudSat. *Journal of Geophysical Research: Atmospheres*, **118**, 10–082.
- 536 Sahany, S., Venugopal, V. and Nanjundiah, R. S. (2010) Diurnal-scale signatures of monsoon rainfall over the Indian region
537 from TRMM satellite observations. *Journal of Geophysical Research: Atmospheres*, **115**.
- 538 Sharma, N., Attada, R. and Hunt, K. M. R. (2021) Evaluating winter precipitation over the western himalayas in high resolution
539 Indian regional reanalysis using multi-source climate datasets. In preparation.
- 540 Shrestha, D., Singh, P. and Nakamura, K. (2012) Spatiotemporal variation of rainfall over the central Himalayan region revealed
541 by TRMM Precipitation Radar. *Journal of Geophysical Research: Atmospheres*, **117**.
- 542 Singh, R., Thapliyal, P. K., Kishtawal, C. M., Pal, P. K. and Joshi, P. C. (2007) A new technique for estimating outgoing longwave
543 radiation using infrared window and water vapor radiances from Kalpana very high resolution radiometer. *Geophysical*
544 *Research Letters*, **34**.
- 545 Tang, G.-Q., Clark, M. P., Papalexiou, S. M., Ma, Z.-Q. and Hong, Y. (2020) Have satellite precipitation products improved
546 over last two decades? A comprehensive comparison of GPM IMERG with nine satellite and reanalysis datasets. *Remote*
547 *Sensing of Environment*, **240**, 111697.
- 548 Turner, A. G., Bhat, G. S., Martin, G. M., Parker, D. J., Taylor, C. M., Mitra, A. K., Tripathi, S. N., Milton, S., Rajagopal, E. N., Evans,
549 J. G. et al. (2020) Interaction of Convective Organisation with Monsoon Precipitation, Atmosphere, Surface and Sea: the
550 2016 INCOMPASS field campaign in India. *Quarterly Journal of the Royal Meteorological Society*, **146**, 2828–2852.
- 551 Ueno, K., Kayastha, R. B., Yasunari, T., Nakawo, M. and Chitrakar, M. R. (2001) Meteorological observations during 1994–2000
552 at the automatic weather station (GEN-AWS) in Khumbu region, Nepal Himalayas. *Bulletin of Glaciological Research*, **18**,
553 23–30.
- 554 Watters, D., Battaglia, A. and Allan, R. P. (2021) The diurnal cycle of precipitation according to multiple decades of global
555 satellite observations, three CMIP6 models, and the ECMWF reanalysis. *Journal of Climate*, **34**, 5063–5080.

- 556 de Wekker, S. F. J., Zhong, S., Fast, J. D. and Whiteman, C. D. (1998) A numerical study of the thermally driven plain-to-basin
557 wind over idealized basin topographies. *Journal of Applied Meteorology and Climatology*, **37**, 606–622.
- 558 Yashiro, H., Kajikawa, Y., Miyamoto, Y., Yamaura, T., Yoshida, R. and Tomita, H. (2016) Resolution dependence of the diurnal
559 cycle of precipitation simulated by a global cloud-system resolving model. *Sola*, **12**, 272–276.

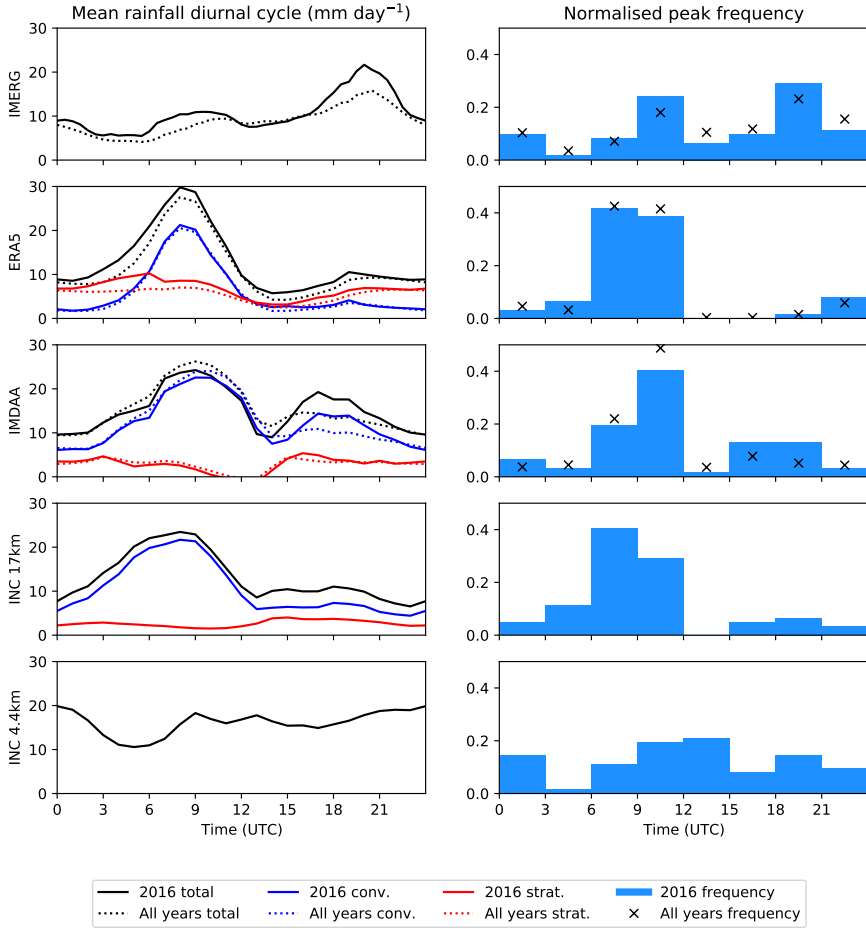


FIGURE 12 Comparison of diurnal cycle of precipitation over the study region in GPM-IMERG, ERA5 and IMDAA reanalyses, and two resolutions (17 km with parameterised convection; 4.4 km with explicit convection) of a limited area MetUM experiment simulating the 2016 season. Left: the mean Jul-Aug diurnal cycle (for 2016 with solid lines, for all available years with dotted lines), with convective (blue) and large-scale (red) contributions if available. Right: the relative frequency of days with a diurnal peak occurring in the given three-hourly bins is plotted (2016 with blue bars, all available years with black crosses).